Computational Mechanics
https://doi.org/10.1007/s00466-019-01717-z

ORIGINAL PAPER

Modeling neurodegeneration in chronic traumatic encephalopathy using gradient damage models

L. Noël[1] · E. Kuhl[1]

Received: 3 October 2018 / Accepted: 30 April 2019
© Springer-Verlag GmbH Germany, part of Springer Nature 2019

Abstract
Chronic traumatic encephalopathy is a progressive neurodegenerative disorder that results from repetitive impacts to the head. Its distinguishing feature is an accumulation of abnormal tau proteins in characteristic regions within the brain. Histopathological studies reveal that tau consistently localizes at the depth of cerebral sulci; yet, the mechanistic origin of this pattern remains unclear. Here we show that a continuum damage model, enhanced with nonlocal gradients, can explain the initial distribution of abnormal tau proteins. We hypothesize that tau aggregation is associated with neuronal death, which we represent as tissue softening and stiffness degradation. Our simulations correctly identify the initial locations of tau deposition, at the depth of cerebral sulci, from where damage spreads within the cortical layer and then across the entire brain. Our computational model has the potential to provide a mechanistic explanation of the stereotypic histopathology of chronic traumatic encephalopathy and predict the cumulative effects of repeated mild traumatic brain injuries.

Keywords Chronic traumatic encephalopathy · Mild traumatic brain injury · Continuum damage mechanics · Gradient damage · Finite element modeling

1 Motivation

Traumatic brain injuries constitute a growing health issue worldwide [30]. Following extensive media coverage of sport-related head injuries, traumatic brain injuries gained an increased attention in the scientific community over the past few years [21,40]. Chronic traumatic encephalopathy is a progressive neurodegenerative disease that affects patients at an early age and is caused by repetitive mild traumatic brain injuries. Chronic traumatic encephalopathy shares many features with other pathologies, but is specific in the sense that it results from a combination of both short-term biomechanical damage and long-term biochemical damage [43]. The early stages of the disease are characterized by highly localized impaired areas, potentially presenting axonal failure, similar to acute traumatic brain injury [21], while the later stages appear more similar to long-term neurodegenerative pathologies such as Alzheimer's disease [5].

From a histopathological point of view, chronic traumatic encephalopathy manifests itself by an accumulation of abnormally phosphorylated tau proteins within the brain [29]. In the healthy brain, tau proteins interact and help stabilizing axonal microtubules, which are responsible for the structural stability and the intracellular transport in the axons [11]. High strains and strain rates cause tau proteins to loose part of their ability to link to microtubules and to misfold into so-called neurofibrillary tangles [41]. The loss of stabilizing tau proteins triggers the depolymerization of microtubules, destabilization of axons, loss of axonal transport, and, eventually, cell death [10].

Figure 1 shows post-mortem immunostaining of brain tissues affected by chronic traumatic encephalopathy, where tau protein tangles have accumulated at the depth of cortical sulci and around blood vessels [28]. Chronic traumatic encephalopathy is a progressive pathology that develops over a long-time span. In the early stage, tau protein tangles accumulate in localized areas. Then, misfolded proteins propagate to connected regions and gradually spreads across the whole brain [46]. The last stage of the disease is associated with structural degradation and brain atrophy [19]. Figure 2 highlights the successive stereotypic stages of chronic traumatic encephalopathy [28].

✉ E. Kuhl
ekuhl@stanford.edu
http://biomechanics.stanford.edu

[1] Department of Mechanical Engineering, Stanford University, Stanford, CA 94305, USA

Published online: 15 May 2019

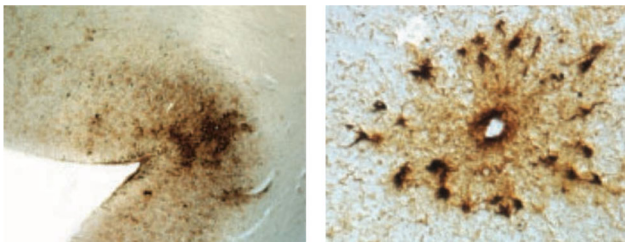

Fig. 1 Characteristic histopathological features of chronic traumatic encephalopathy. Damage, indicated through the aggregation of misfolded tau proteins, is first visible at the depth of cerebral sulci, left, and around small blood vessels, right; adapted with permission [28]

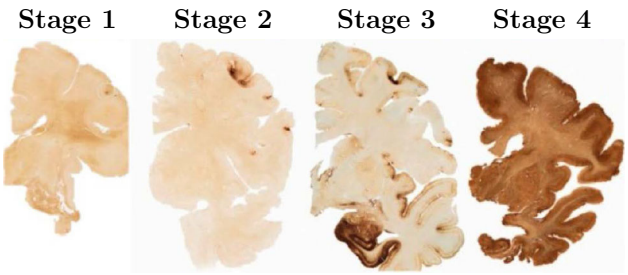

Fig. 2 Characteristic progressive stages of chronic traumatic encephalopathy. Damage begins through the focal accumulation of tau protein tangles at the depth of cerebral sulci (Stage 1); then protein misfolding propagates from the initial punctual locations to the closely surrounding cortex (Stage 2); until misfolded tau proteins are broadly spread across the brain (Stage 3); ultimately tau pathology affects the entire cerebral cortex and triggers brain atrophy (Stage 4); adapted with permission [28]

Since the accumulation of tau is associated with cognitive impairment, tau holds promise as an early biomarker for neurodegeneration. Current research efforts are underway to selectively image tau in vivo and develop tau tracers for positron emission tomography [44]. While the in vivo detection of misfolded tau proteins remains challenging, the technique should enable early diagnosis of the disease and close monitoring of its progression. Yet, to date, the only reliable tool to diagnose chronic traumatic encephalopathy is post-mortem histopathology [29], similar to Fig. 1. Computational simulations could help address this challenge and provide insight into the complex initiation and propagation of neurodegeneration across the brain.

Initially focusing on acute traumatic brain injury, computational simulations aimed at determining damage predictors and injury level thresholds for brain tissue impairment. These thresholds were correlated with experimental data from animal models [49]. Strain and strain rate levels were identified to predict brain tissue degradation. To calibrate a widely used head injury criterion, studies characterized the effects of impact loading on two-dimensional transversal brain slices [32]. The highly localized initiation of tissue impairment in traumatic brain injury supported the hypothesis that the brain convoluted geometry played an important role in damage accumulation. By accounting for brain morphology, numerical simulations confirmed that the brain mechanical response to various loading scenarios was maximal in specific locations, as observed in practice. While initial studies investigated the influence of brain morphology on its mechanical response to head rotations in idealized two-dimensional brain slices [7], more sophisticated analyses used three-dimensional brain models extracted from magnetic resonance images [20]. Recent studies predicted the initial location of damage using high fidelity three-dimensional brain models exposed to high impact loading [16].

Most brain injury models focus on the immediate response using elastic or viscoelastic constitutive models [8]. While elasticity and viscoelasticity seem reasonable to explore injury level thresholds in response to a *single severe* traumatic brain injury, they cannot account for the progressive degeneration in response to *several moderate* traumatic brain injuries during which the tissue might be irreversibly impaired [19]. As Fig. 2 suggests, degradation starts spreading from these initial damaged locations, which are strongly degraded in the final stage of the pathology [28]. There is a general agreement that the functional degradation of brain tissue is closely related to its structural degradation and, ultimately, to cerebral softening [18]. Encephalomalacia is one form of cerebral softening that can result from cerebral infarction, cerebral ischemia, or traumatic brain injury [23]. Previous studies have measured brain tissue softening in response to brain tissue damage ex vivo [13] and visualized encephalomalacia with magnetic resonance imaging in vivo [37]. Magnetic resonance elastography now allows us to quantify brain tissue softening in response to brain damage non-invasively in vivo [47] and could serve as a biomarker to monitor the progression of injury-induced cerebral softening both in space and time.

Here we model the irreversible behavior of the brain tissue using continuum damage mechanics [26] to better understand the initiation and propagation of chronic traumatic encephalopathy. Recent studies have shown that continuum damage mechanics is a powerful tool to explain the gradual structural degeneration on the axonal level [9] and on the tissue level [15]. We focus on the early stages of damage, the initiation of neurodegeneration within the brain, and on the biomechanical aspects of tissue degradation [18]. First, we confirm previous results related to the location of the initial degeneration [29]. Then, we simulate the gradual accumulation of misfolded tau proteins using the standard concepts of continuum damage mechanics [39] enhanced by local gradient terms [33]. Since neurofibrillary tangles have a disruptive effect on axonal stability and eventually lead to cell death, we assume that the deposition of misfolded proteins is associated with a softening behavior of the tissues. Inspired by classi-

cal damage mechanics, we model this structural degradation through a single scalar-valued damage variable.

The remainder of his manuscript is organized as follows. Section 2 briefly describes the continuum damage model used to describe the irreversible brain tissue behavior. As damage is a strain softening phenomenon, a gradient enhanced approach is exploited to regularize the problem and its numerical implementation is recalled. Section 3 focuses on the brain model. Idealized two-dimensional brain slices are considered and their geometries and properties are detailed. Section 4 first illustrates the damage model and the effect of the associated regularization, then gathers numerical results obtained from linear acceleration loading scenarios on two-dimensional brain slices. Finally, the limitations and perspectives offered by the proposed damage framework are discussed in Sect. 5.

2 Methods

2.1 Continuum damage model

We characterize brain tissue through an isotropic continuum damage model in terms of the strain energy per unit undeformed volume [38,39],

$$\Psi = [\,1 - d\,]\, W\,, \tag{1}$$

where d is a scalar damage value and W is the elastic strain energy. Damage evolves gradually from the undamaged state, $d = 0$, towards the fully damaged state, $d = 1$. We select an exponential type damage evolution law [18],

$$d = \exp\left(-\exp\left[\eta\,(\kappa_1 - \kappa)\right]\right)\,, \tag{2}$$

where the internal variable κ keeps track of the maximum nonlocal elastic strain energy $\bar{W}$ throughout the loading history,

$$\kappa = \max_{-\infty<\tau<t}\left\{\bar{W}(\tau),\,\kappa_0\right\}\,, \tag{3}$$

the parameter η defines the slope of the damage evolution and κ_0 and κ_1 are damage thresholds beyond which damage occurs. This damage law closely mimics the available experimental data [2], and can account for an initial baseline damage $d > 0$ at $\bar{W} = 0$, that is not mechanically induced, but, for example, age-related. We further specify the meaning and values of these parameters in Sect. 3. In the discrete finite element setting, strain softening behavior generally leads to strain localization and a spurious mesh sensitivity [4]. To avoid these issues, different regularization approaches, relying on the introduction of an internal length scale, have been proposed [25]. Here we adopt an implicit definition of the nonlocal strain energy $\bar{W}$,

$$\overline{W} - l_0^2\,\mathrm{Div}(\nabla\overline{W}) \doteq W\,, \tag{4}$$

by averaging the local strain energy W over a domain characterized by a length l_0 in the reference domain $\mathcal{B}_0$ [42]. We assume a strain energy function W of neo-Hookean type,

$$W = \frac{1}{2}\,\lambda\ln^2(J) + \frac{1}{2}\,\mu\,[\boldsymbol{F}:\boldsymbol{F} - n_{\mathrm{dim}} - 2\ln(J)]\,. \tag{5}$$

Here,

$$\boldsymbol{F} = \nabla\boldsymbol{\varphi} \quad \text{and} \quad J = \det(\boldsymbol{F})\,, \tag{6}$$

are the deformation gradient and the Jacobian, n_{dim} is the number of spatial dimensions, and λ and μ are the Lamé coefficients, which, in the limit case of small deformations, translate into Young's modulus E and Poisson ratio ν as,

$$\lambda = \frac{E\nu}{[1+\nu][1-2\nu]} \quad \text{and} \quad \mu = \frac{E}{2[1+\nu]}\,. \tag{7}$$

Throughout the entire loading history, we solve the balance of linear momentum,

$$\mathrm{Div}(\boldsymbol{P}) \doteq \boldsymbol{f} \tag{8}$$

the equilibrium between the internal forces, the divergence of the Piola stress, $\mathrm{Div}(\boldsymbol{P})$, and the external forces, $\boldsymbol{f}$. The total Piola stress, $\boldsymbol{P} = \partial\Psi/\partial\boldsymbol{F}$, and its elastic counterpart, $\boldsymbol{P}^{\mathrm{e}} = \partial W/\partial\boldsymbol{F}$, follow as

$$\boldsymbol{P} = [\,1-d\,]\boldsymbol{P}^{\mathrm{e}} \;\text{ with }\; \boldsymbol{P}^{\mathrm{e}} = \mu\,\boldsymbol{F} + [\,\lambda\ln(J) - \mu\,]\boldsymbol{F}^{-\mathrm{t}}. \tag{9}$$

2.2 Computational damage model

To solve the mechanical equilibrium equation (8) and the nonlocal strain energy equation (4), we translate them into their residual forms,

$$\begin{aligned} \mathbf{R}^{\varphi} &= \mathrm{Div}(\boldsymbol{P}) - \boldsymbol{f} \doteq \mathbf{0}\,,\\ \mathrm{R}^{\overline{W}} &= l_0^2\mathrm{Div}(\nabla\overline{W}) - \overline{W} + W \doteq 0\,. \end{aligned} \tag{10}$$

We discretize the domain of interest, $\mathcal{B}_0 = \mathsf{U}_{e=1}^{n_{el}}\mathcal{B}_0^e$ by n_{el} finite elements and we interpolate the deformation $\boldsymbol{\varphi}$, the nonlocal energy $\overline{W}$, and their test functions $\delta\boldsymbol{\varphi}$ and $\delta\overline{W}$ by their nodal values $\boldsymbol{\varphi}_k$, $\overline{W}_l$, $\delta\boldsymbol{\varphi}_i$ and $\delta\overline{W}_j$ with the element shape functions N^{φ} and $N^{\overline{W}}$,

$$\begin{aligned} \delta\boldsymbol{\varphi} &= \sum_i N_i^{\varphi}\,\delta\boldsymbol{\varphi}_i \quad \text{and} \quad \boldsymbol{\varphi} = \sum_k N_k^{\varphi}\,\boldsymbol{\varphi}_k\,,\\ \delta\overline{W} &= \sum_j N_j^{\overline{W}}\,\delta\overline{W}_j \quad \text{and} \quad \overline{W} = \sum_l N_l^{\overline{W}}\,\overline{W}_l\,, \end{aligned} \tag{11}$$

where i, j, k, l are the local element nodes. To avoid stress oscillations, we choose quadratic interpolation functions for the displacement field and linear interpolation functions for

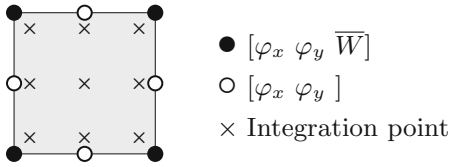

Fig. 3 Discretization fields and associated degrees of freedom on a quadrangular element

the nonlocal strain energy field, i.e., $i,k = 1,\dots,8$ and $j,l = 1,\dots,4$ as in Peerlings et al. [34]. Figure 3 illustrates the resulting degrees of freedom for one element. We assume a plane strain state [17] and perform a full integration with 3 $\times$ 3 integration points per element.

We apply Dirichlet boundary conditions for the mechanical equilibrium problem (10.1), $\boldsymbol{\varphi} = \overline{\boldsymbol{\varphi}}$, and homogeneous Neumann boundary conditions for the nonlocal energy problem (10.2), $\nabla\overline{W}\cdot\boldsymbol{N} = 0$, where $\boldsymbol{N}$ is the outward unit normal vector in the reference domain. Integrating the residuals (10) over the domain of interest $\mathcal{B}_0$, multiplying them with the test functions $\delta\boldsymbol{\varphi}$ and $\delta\overline{W}$ (11), and integrating their first terms by parts, yields the weak form of the governing equations,

$$\begin{aligned}
\mathbf{R}^{\varphi}_I &= \mathop{\mathbf{A}}_{e=1}^{n_{el}} \int_{\mathcal{B}^e_0} \nabla N^{\varphi}_I \cdot \boldsymbol{P} + N^{\varphi}_I\, \boldsymbol{f}\, \mathrm{d}V_e \doteq \mathbf{0}\,,\\
\mathsf{R}^{\overline{W}}_J &= \mathop{\mathbf{A}}_{e=1}^{n_{el}} \int_{\mathcal{B}^e_0} \nabla N^{\overline{W}}_J \cdot l_0^2\, \nabla\overline{W} + N^{\overline{W}}_J\, [\overline{W} - W]\, \mathrm{d}V_e \doteq 0.
\end{aligned} \tag{12}$$

Here, the operator $\mathbf{A}_{e=1}^{n_{el}}$ denotes the assembly of all local element nodes i and j to the global nodes I and J. To solve the coupled nonlinear set of equations (12), we adopt an incremental iterative scheme and linearize the equations,

$$\begin{aligned}
\mathbf{R}^{\varphi}_I + \sum_K \mathbf{K}^{\varphi\varphi}_{IK}\, \mathrm{d}\boldsymbol{\varphi}_K + \sum_L \mathbf{K}^{\varphi\overline{W}}_{IL}\, \mathrm{d}\overline{W}_L &\doteq 0,\\
\mathsf{R}^{\overline{W}}_J + \sum_K \mathbf{K}^{\overline{W}\varphi}_{JK}\, \mathrm{d}\boldsymbol{\varphi}_K + \sum_L \mathsf{K}^{\overline{W}\overline{W}}_{JL}\, \mathrm{d}\overline{W}_L &\doteq 0.
\end{aligned} \tag{13}$$

with the following contributions to the global tangent matrix,

$$\begin{aligned}
\mathbf{K}^{\varphi\varphi}_{IK} &= \frac{\mathrm{d}\mathbf{R}^{\varphi}_I}{\mathrm{d}\boldsymbol{\varphi}_K} = \mathop{\mathbf{A}}_{e=1}^{n_{el}} \int_{\mathcal{B}^e_0} \nabla N^{\varphi}_I \cdot \frac{\mathrm{d}\boldsymbol{P}}{\mathrm{d}\boldsymbol{F}} \cdot \nabla N^{\varphi}_K\, \mathrm{d}V_e\,,\\
\mathbf{K}^{\varphi\overline{W}}_{IL} &= \frac{\mathrm{d}\mathbf{R}^{\varphi}_I}{\mathrm{d}\overline{W}_L} = \mathop{\mathbf{A}}_{e=1}^{n_{el}} \int_{\mathcal{B}^e_0} -\nabla N^{\varphi}_I \cdot \frac{\mathrm{d}d}{\mathrm{d}\overline{W}} \boldsymbol{P}^{\mathrm{e}}\, N^{\overline{W}}_L\, \mathrm{d}V_e\,,\\
\mathbf{K}^{\overline{W}\varphi}_{JK} &= \frac{\mathrm{d}\mathsf{R}^{\overline{W}}_J}{\mathrm{d}\boldsymbol{\varphi}_K} = \mathop{\mathbf{A}}_{e=1}^{n_{el}} \int_{\mathcal{B}^e_0} -N^{\overline{W}}_J\, \boldsymbol{P}^{\mathrm{e}} \cdot \nabla N^{\varphi}_K\, \mathrm{d}V_e\,,\\
\mathsf{K}^{\overline{W}\overline{W}}_{JL} &= \frac{\mathrm{d}\mathsf{R}^{\overline{W}}_J}{\mathrm{d}\overline{W}_L} = \mathop{\mathbf{A}}_{e=1}^{n_{el}} \int_{\mathcal{B}^e_0} N^{\overline{W}}_J\, N^{\overline{W}}_L + \nabla N^{\overline{W}}_J \cdot l_0^2\, \nabla N^{\overline{W}}_L\, \mathrm{d}V_e.
\end{aligned} \tag{14}$$

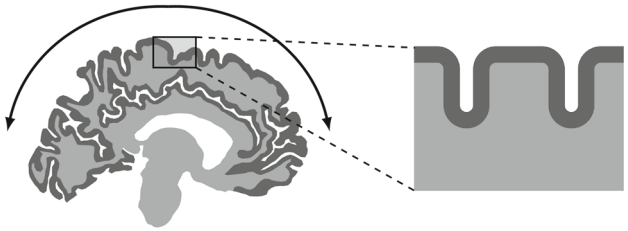

Fig. 4 Head rotations as injury mechanisms in chronic traumatic encephalopathy: modeling the mechanical response of a brain slice

The fourth order tensor of the damage moduli is

$$\begin{aligned}
\frac{\mathrm{d}\boldsymbol{P}}{\mathrm{d}\boldsymbol{F}} = [\,1-d\,]\big[\,&\lambda\, \boldsymbol{F}^{-\mathrm{t}} \otimes \boldsymbol{F}^{-\mathrm{t}} + \mu\, \boldsymbol{I} \,\overline{\otimes}\, \boldsymbol{I}\\
&+[\,\mu - \lambda \ln(J)\,]\, \boldsymbol{F}^{-\mathrm{t}} \underline{\otimes} \boldsymbol{F}^{-1}\big]\,,
\end{aligned} \tag{15}$$

where the components of the following fourth-order products are $\{\bullet \,\overline{\otimes}\, \circ\}_{ijkl} = \{\bullet\}_{ik}\{\circ\}_{jl}$ and $\{\bullet \,\underline{\otimes}\, \circ\}_{ijkl} = \{\bullet\}_{il}\{\circ\}_{jk}$. The derivative of the damage value with respect to the nonlocal strain energy is

$$\frac{\mathrm{d}d}{\mathrm{d}\overline{W}} = \eta\, d\, \exp(\eta\,[\kappa_1 - \kappa\,])\,. \tag{16}$$

3 Brain model

In this study, we focus on head rotations as loading scenarios since rotational accelerations are considered a major injury mechanism in traumatic brain injury and chronic traumatic encephalopathy [21].

Figure 4 illustrates our idealized model problem to systematically investigate the effect of head rotations [7]. We model a two-dimensional representative section of the brain that is 30 mm long and 20 mm high and includes both gray matter, represented as a 2.5 mm thick upper layer and white matter as the underlying substrate.

Figure 5 illustrates our loading conditions. We focus on linear acceleration loadings. For simplicity, we restrict ourselves to a quasi-static analysis and apply accelerations as equivalent forces, $\boldsymbol{f}_I = \rho_0 \sum_i N^{\varphi}_i\, \ddot{\overline{\boldsymbol{\varphi}}}_i$, which we interpolate from the prescribed nodal accelerations $\ddot{\overline{\boldsymbol{\varphi}}}$ using the interpolation functions N^{φ}_i and the density ρ_0. For the deformation field, we apply periodic Dirichlet boundary conditions at the left and right boundaries, enforce zero Dirichlet boundary conditions at the bottom, and apply zero Neumann boundary conditions along the folds at the top. For the nonlocal energy field, we apply vanishing Neumann boundary conditions along the entire boundary.

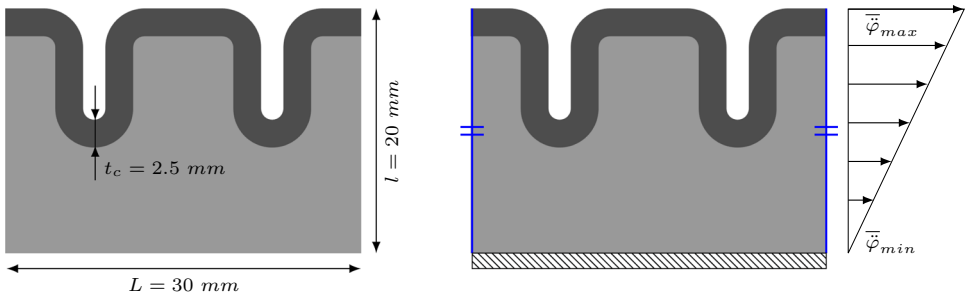

Fig. 5 Two-dimensional brain model with two sulci and three gyri. Dimensions, left, and boundary and loading conditions, right

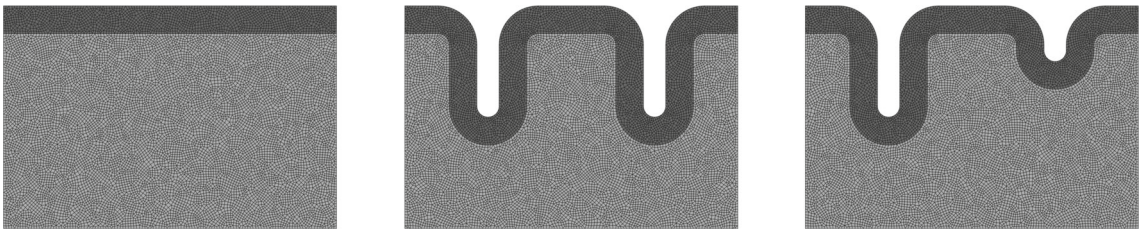

Fig. 6 Two-dimensional brain model, geometries, and meshes. Smooth surface, left, two equivalent sulci, center, and one deep and one shallow sulcus, right

Figure 6 shows our two model systems: one with two equivalent sulci and one with a deep and a shallow sulcus. We discretize the first system with 11,500 and the second with 11,699 quadrilateral finite elements, corresponding to 3438 and 2941 elements for the gray matter layer and 8062 and 8758 elements for the white matter substrate. This results in discretizations with 93,612 and 95,084 degrees of freedom, of which 70,074 and 71,188 are associated with the deformation and 23,538 and 23,896 with the nonlocal energy.

3.1 Model parameters

We model gray and white matters as neo-Hookean materials, as expressed in Eq. (5). Table 1 summarizes the material parameters of our brain model [6]. The subscripts w and g indicate the white and gray matter. We calibrate our damage law using in vivo experiments on guinea pigs optical nerves [2]. The study reports three injury thresholds in terms of the Green-Lagrange strain, the conservative threshold of 0.14 at which all axons are still intact, the liberal threshold of 0.34 at which all axons are fully damaged, and the optimal threshold of 0.21 at which axons transition between intact and damaged. Figure 7 illustrates our exponential damage law, as defined in Eq. (2), calibrated to interpolate these three data points [18]. Since gray and white matter tissues present different microstructures, they might exhibit a different damage behavior and, with it, different damage parameters. Unfortunately, as experimental results on damage are only available for white matter in the literature, we assume that both gray and white matters are characterized by the same damage threshold values. Table 2 summarizes the corresponding damage parameters.

Table 1 Brain model—elastic material parameters

Parameters	Values	Units	References
Stiffness			
μ_w	1.15	kPa	[6]
ν_w	0.45	–	
μ_g	2.07	kPa	
ν_g	0.45	–	
Density			
ρ_g	1040	kg/m^3	[3]
ρ_w	1040	kg/m^3	

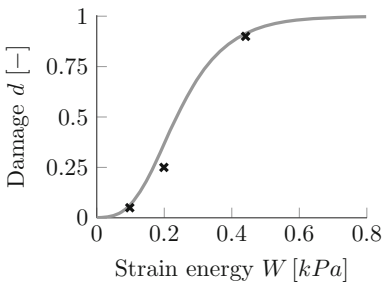

Fig. 7 Damage model parameterized in terms of the strain energy. The three crosses represent three strain-based damage thresholds [2], the solid line their interpolation using an exponential damage law [18]

4 Results

4.1 Model illustration and sensitivity analyses

First, we illustrate the damage model and the effects of its nonlocal regularization. Figure 8 shows our idealized two-

Table 2 Brain model—damage material parameters

Parameters	Values	Units	References
Damage thresholds			
κ_0	0.0	kPa	[2]
κ_1	0.2	kPa	
Damage slope			
η	10	kPa^{-1}	

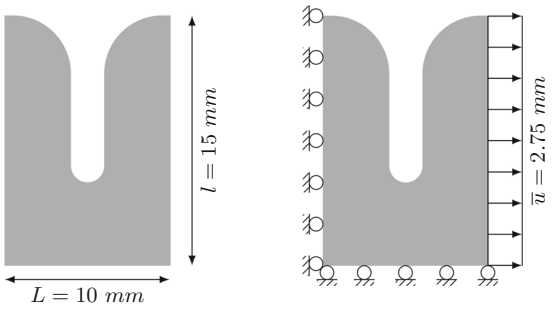

Fig. 8 Two-dimensional model system with one sulcus and two gyri to demonstrate the nonlocal effects and calibrate the damage model. Dimensions, left, and loading conditions, right

dimensional model system, 10 mm long and 15 mm high, made of white matter only. Motivated by similar studies in the literature [7], we fix the horizontal and the vertical displacements of the model at its left and bottom boundaries, respectively, and prescribe the horizontal displacements on the right boundary, see Fig. 8. We solve the linearized system of equations (13) using a displacement-controlled Newton-Raphson scheme. We define the convergence threshold as a residual norm of 10^{-5} relative to its initial value.

4.1.1 Example 1: sensitivity with respect to mesh size

This first example demonstrates the ability of the regularization to achieve mesh-independent results. We discretize the slice in Fig. 8 with 716, 2735 and 10562 quadrilateral finite elements, corresponding to mesh sizes of $h = 0.5$ mm, 0.25 mm, and 0.125 mm, respectively. For this example, we select a constant internal length of $l_0 = 1.5$ mm. Figure 9 shows the local strain energy, the nonlocal strain energy, and the damage fields for the three different discretizations on the deformed configuration. Figure 10 summarizes the corresponding force-displacement curves for the three simulations. The reaction forces are normalized with respect to the maximum value reached during the loading history for each simulation. These results confirm the efficiency of the nonlocal regularization as the structural response is independent of the mesh size. For each mesh, the maximal nonlocal strain values as well as the damage areas are similar. The force-displacement curves for the three discretizations are virtually overlapping.

4.1.2 Example 2: sensitivity with respect to internal length scale

This second example investigates the influence of the internal length parameter l_0. We consider three internal lengths, $l_0 = 1.5$ mm, 2 mm, and 2.5 mm, while keeping the mesh size fixed at $h = 0.25$ mm. Choosing the internal length scale has been a matter of ongoing debate in nonlocal and gradient continuum theories. In theory, we could determine the internal length scale through inverse analysis and parameter identification [27]. In practice, the internal length scale is likely related to a microstructural length, for example, the size of a neuron [14]. Unfortunately, up to date, there are no experimental data that characterize this length scale. Here, we select an internal length that is smaller than the cortical thickness. This provides physiologically realistic results in accordance with histological observations, which have shown that damage develops in and is initially constrained to the cortical layer. Figure 11 shows the local strain energy, the nonlocal strain energy, and the damage fields for the three internal lengths on the deformed configuration. Figure 12 provides the corresponding force-displacement curves. These results show that the structural response is highly dependent on the selected internal length value [1]. Working with larger internal lengths, the areas affected by damage are wider, while the maximal damage value reached drops. The force-displacement curves become steeper and steeper as the internal length value is decreased.

4.1.3 Example 3: sensitivity with respect to stiffness and nonlocal averaging

This example emphasizes the importance of brain tissue material properties and their influence on the mechanical response to external loadings. In the case of nonlocal damage, stiffness heterogeneities have additional implications, which we investigate based on the averaging of the nonlocal degrees of freedom and its impact on the overall response. Since the stiffness values of gray and white matter remain a controversial issue, we consider both, a system in which gray and white matter are equally stiff, $\mu_g = \mu_w = 1.15$ kPa, and a system in which gray matter is 1.8 times stiffer than white matter, $\mu_g = 2.07$ kPa and $\mu_w = 1.15$ kPa [6]. First, we consider a single nonlocal field for the entire domain regardless of the material subdomains. Then we introduce separate nonlocal fields for each material subdomain. For each cases, we use a mesh size fixed at $h = 0.25$ mm. We study three cases: a homogeneous system in which gray and white matter are equally stiff with a single nonlocal field, a heterogeneous system with a stiffer gray matter layer resting on a softer white matter substrate with a single nonlocal field for both subdomains, and a similar heterogeneous system but now with separate nonlocal fields for each material

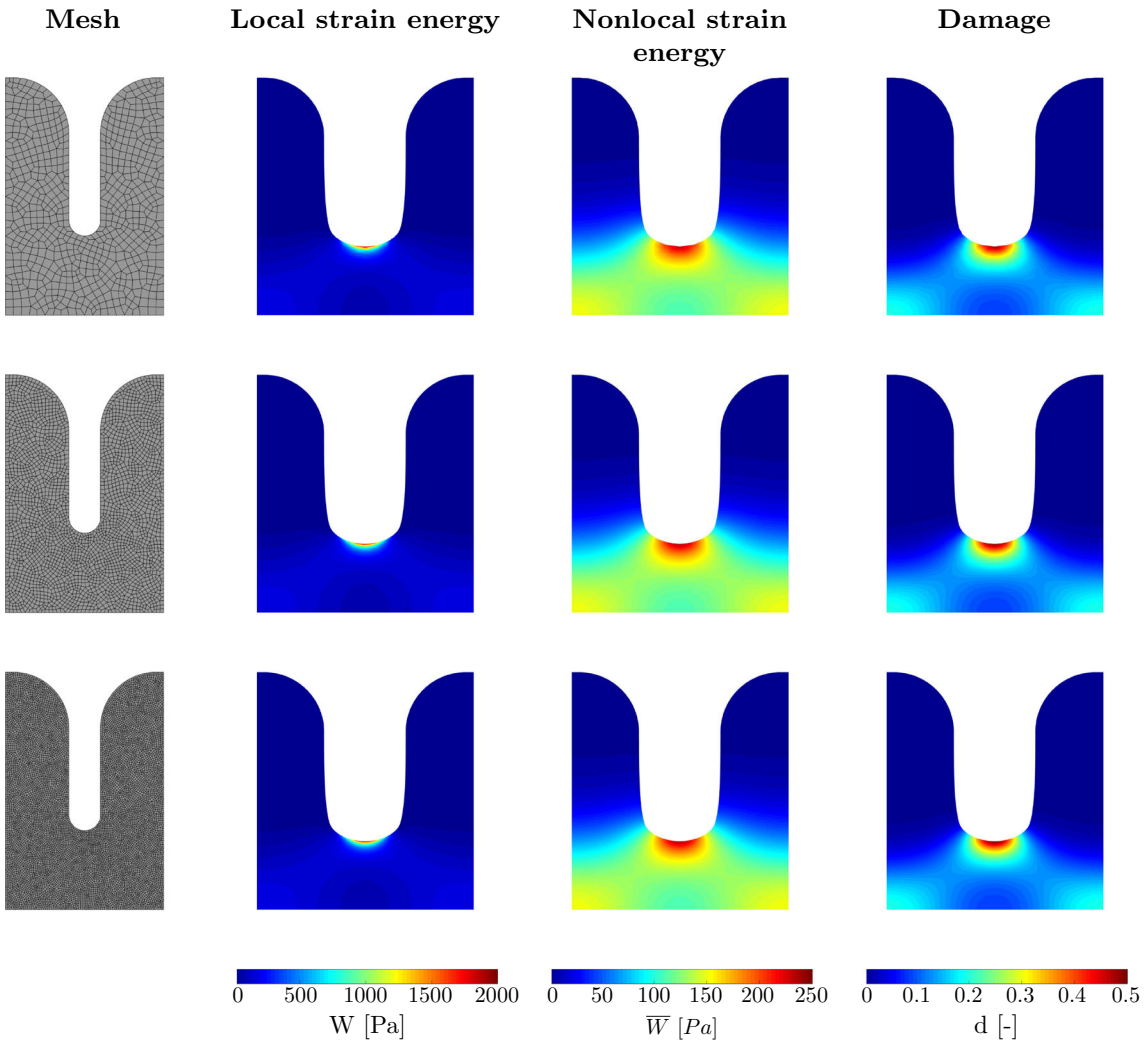

Fig. 9 Influence of the mesh size: local strain energy, nonlocal strain energy, and damage fields on the deformed configuration for three different discretizations with $h = 0.5$ mm, 0.25 mm, and 0.125 mm

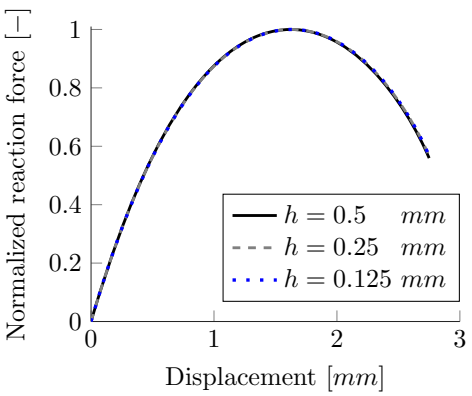

Fig. 10 Influence of the mesh size: force versus displacement curves for three different discretizations $h = 0.5$ mm, 0.25 mm, and 0.125 mm

subdomain. In practice, the first and second case allow damage to propagate from one material to another, while the third case prevents this propagation and confines the strain energy, and with it the damage, to evolve independently in each subdomain. For all three cases we select an internal length of $l_0 = 1$ mm. Figure 13 shows the local strain energy, the nonlocal strain energy, and the damage fields of the three cases described above on the deformed configuration. The first and second cases with a single nonlocal field exhibit similar patterns for the nonlocal strain energy and damage fields. Damage can propagate smoothly from one material to the other. The second and third cases with pronounced stiffness differences have quasi-similar local strain energy fields. They present a similar nonlocal strain energy pattern, but a rather different behavior at the material interface. In fact, the third case is characterized by a discontinuity in the nonlocal strain energy field and generates a confinement of the nonlocal strain energy to each material subdomain and thereby confines damage mainly to the gray matter upper layer. This

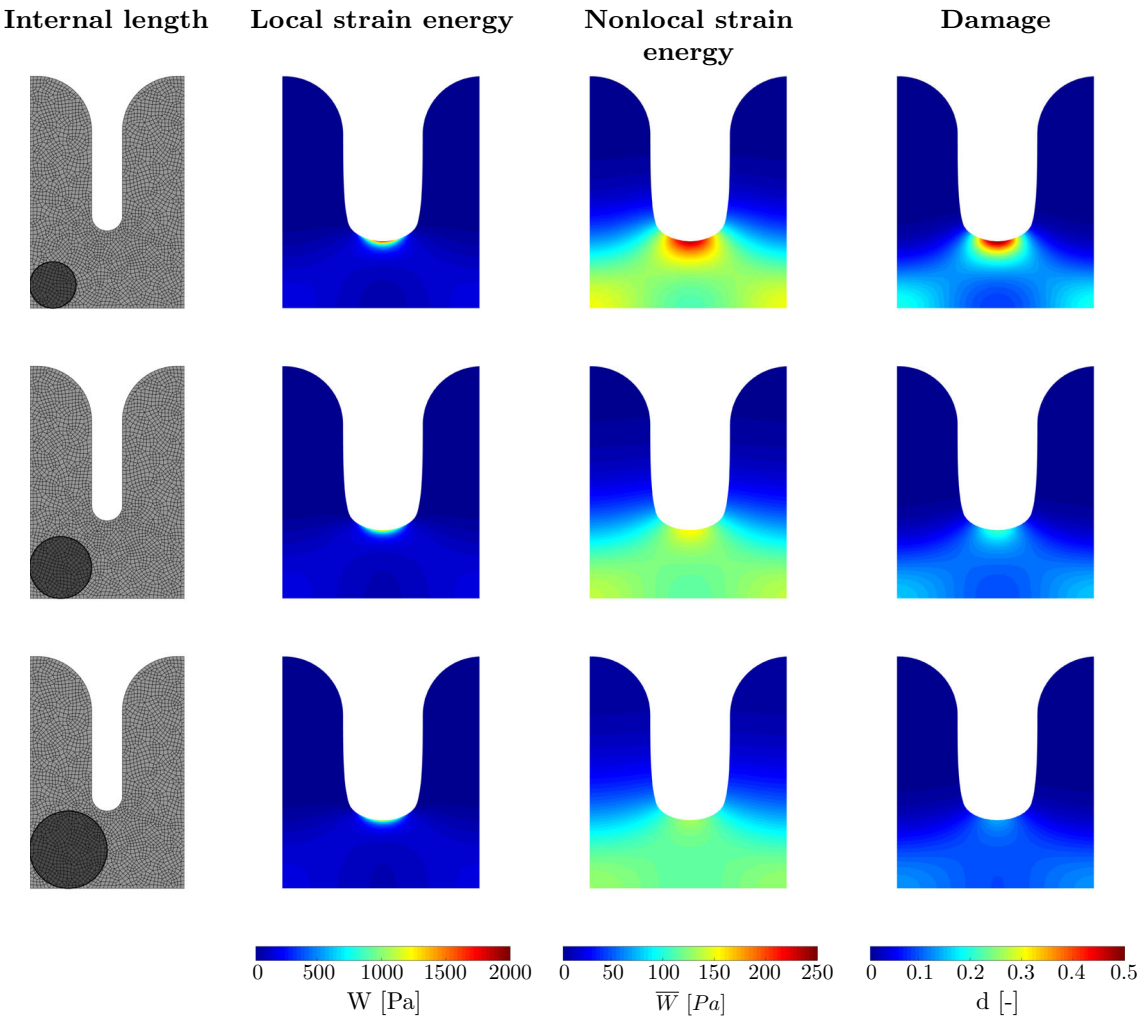

Fig. 11 Influence of the internal length l_0: local strain energy, nonlocal strain energy, and damage fields on the deformed configuration for three different internal length values $l_0 = 1.5$ mm, 2 mm, and 2.5 mm

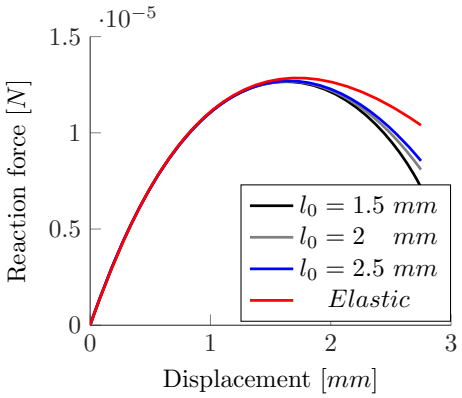

Fig. 12 Influence of the internal length l_0: force versus displacement curves for three different internal length values $l_0 = 1.5$ mm, 2 mm, and 2.5 mm and for the elastic case

situation most closely mimics the observed damage pattern in chronic traumatic encephalopathy, especially in the initial stages where damage initiates at the depth of the cerebral sulci as in Fig. 1. We therefore adopt the third setup in the following examples.

4.2 Brain model examples

This last example focuses on the brain geometry and its influence on the mechanical response to external loadings. We consider three geometries: a system with a smooth surface, a system with two equivalent deep sulci, and a system with one deep and one shallow sulcus, as shown in Fig. 6. In all three cases, we introduce a material interface between gray and white matter and discretize it using a conforming mesh with different material properties in each material. In all three cases, we select an internal length of $l_0 = 1$ mm. We apply acceleration loadings, imposed through static equivalent acceleration forces, and periodic boundary conditions as illustrated in Fig. 5. Since we now prescribe forces instead of displacements, and the damaged brain tissues can exhibit a snap-through or snap-back behavior, we solve the linearized

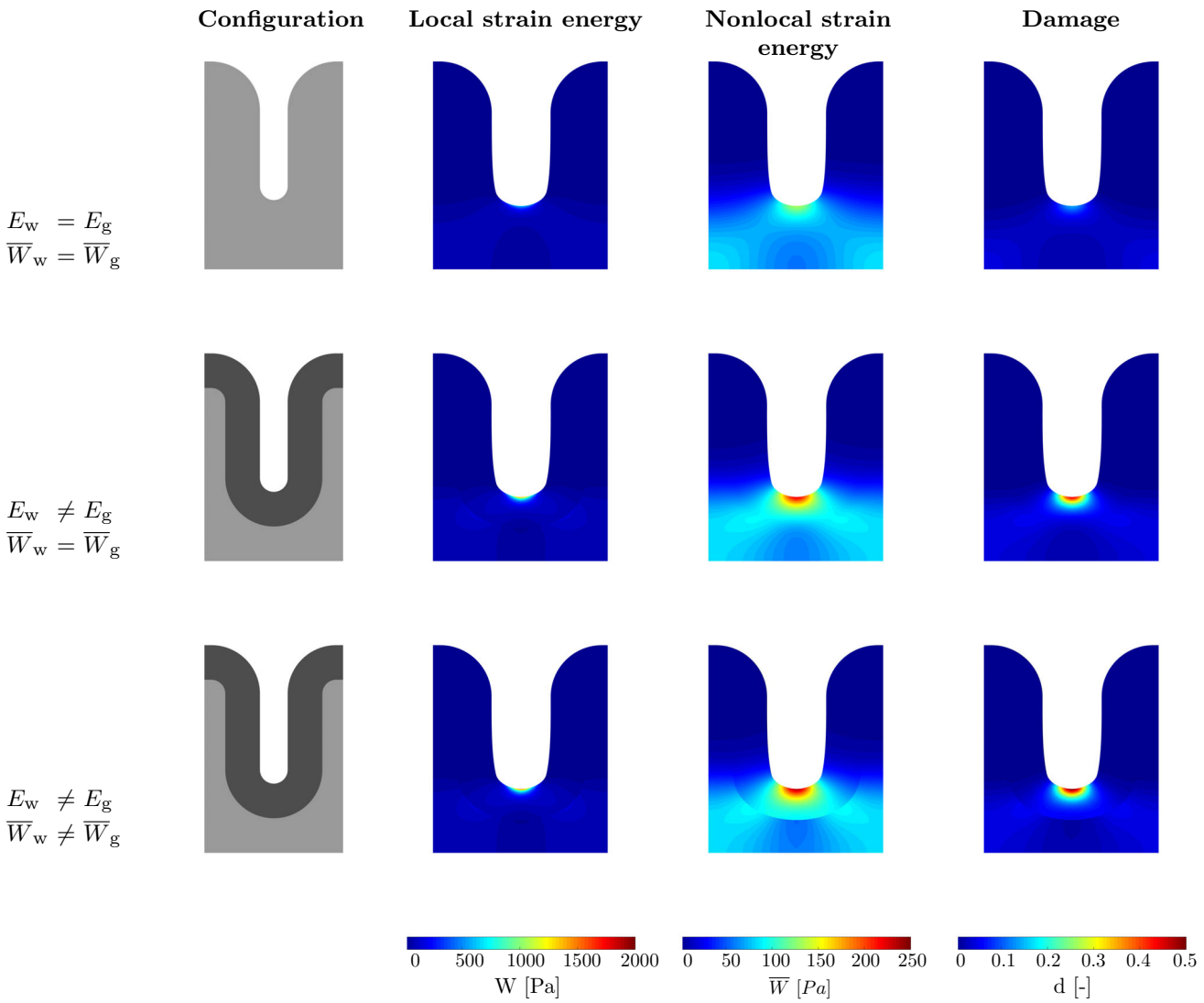

Fig. 13 Influence of a material interface between the upper gray matter layer and the white matter substrate: local strain energy, nonlocal strain energy, and damage fields on the deformed configuration for homogeneous stiffness with a single nonlocal field, heterogeneous stiffness with a single nonlocal field, and heterogeneous stiffness with separate nonlocal fields for each material subdomain

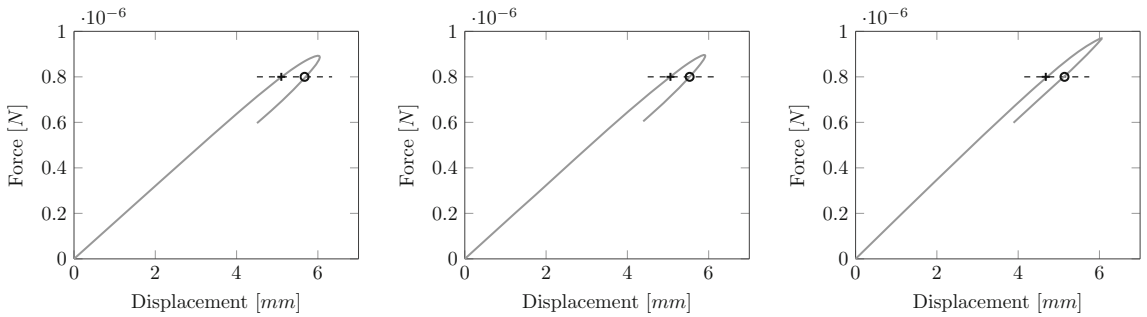

Fig. 14 Influence of brain geometry: force-displacement curves of the upper right corner node of the brain slices for a smooth surface, left, for the two equivalent sulci, center, and the deep and shallow sulcus, right. The cross and circle show the force levels of the snapshots in Figs. 15 and 16

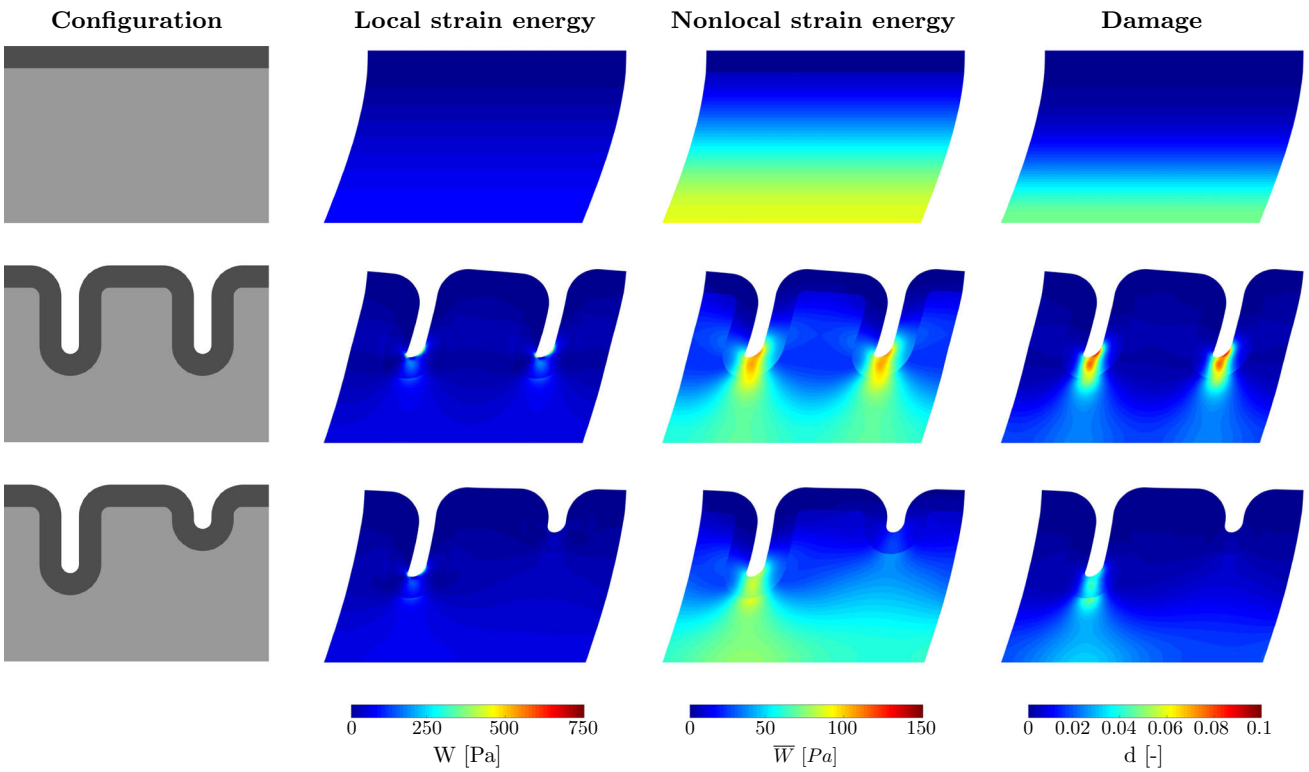

Fig. 15 Influence of brain geometry: local strain energy, nonlocal strain energy, and damage fields for a smooth surface, for two equivalent sulci and for deep and shallow sulci during loading

problem in Eq. (13) using a Riks-Crisfield iteration scheme [36]. At the beginning of the simulation, we compute the equivalent static forces that represent the acceleration pattern in Fig. 5 and then apply those forces incrementally throughout the simulation. We define the convergence threshold as a residual norm of 10^{-5} relative to its initial value. Figures 15 and 16 provide snapshots of the local strain energy, the nonlocal strain energy, and the damage fields for each case at a given force level during both the loading and the unloading stages, as illustrated in Fig. 14. In the first case, strain maxima localize at the bottom of the slice where it is fixed. As a natural consequence of the applied boundary conditions, a distinct damaged layer develops at the bottom of the specimen. In the second case with two equivalent sulci, strain maxima localize at the bottom of the sulci. Damage develops in these localized areas and is mainly confined to the gray cortical layer. Both sulci seem to equally support the load. In the third case with different sulci, strain maxima occur at the depth of the deep sulcus. The deep sulcus undergoes large deformations and the cortex is drastically affected by damage in this location. The deep sulcus shields the shallow sulcus, and both the strain energy and the damage are rather low within that region. For these simulations, we conclude that geometric effects are extremely important in the case of brain damage. The brain's convoluted geometry is not only key for its function, but also influences its mechanical behavior.

5 Discussion

Chronic traumatic encephalopathy is a progressive neurodegenerative disease that develops following repetitive mild traumatic brain injury. The pathology is characterized by an accumulation of tau protein tangles within the brain. Here we use continuum damage mechanics to represent tau inclusions and the subsequent neurodegeneration of the tissues. The main interest of this approach resides in introducing a history dependence in the model to represent the chronic, accumulative, and irreversible nature of neurodegeneration observed under these conditions.

We exploit classical continuum damage mechanics, where damage is represented by a single scalar-valued variable that evolves from zero to one, to represent the gradual degradation of the brain tissue properties. Since damage induces a strain softening behavior, its implementation within numerical methods is associated with strain localization and a spurious mesh dependency [45]. We regularize the problem by introducing a length scale using a gradient enhanced approach [24]. This regularization is particularly well suited to deal with the complex and convoluted geometry of the brain. In contrast to other nonlocal approaches including integral methods, gradient methods avoid spurious interaction between neighboring but disconnected regions [35], which is especially important to avoid averaging across neighbor-

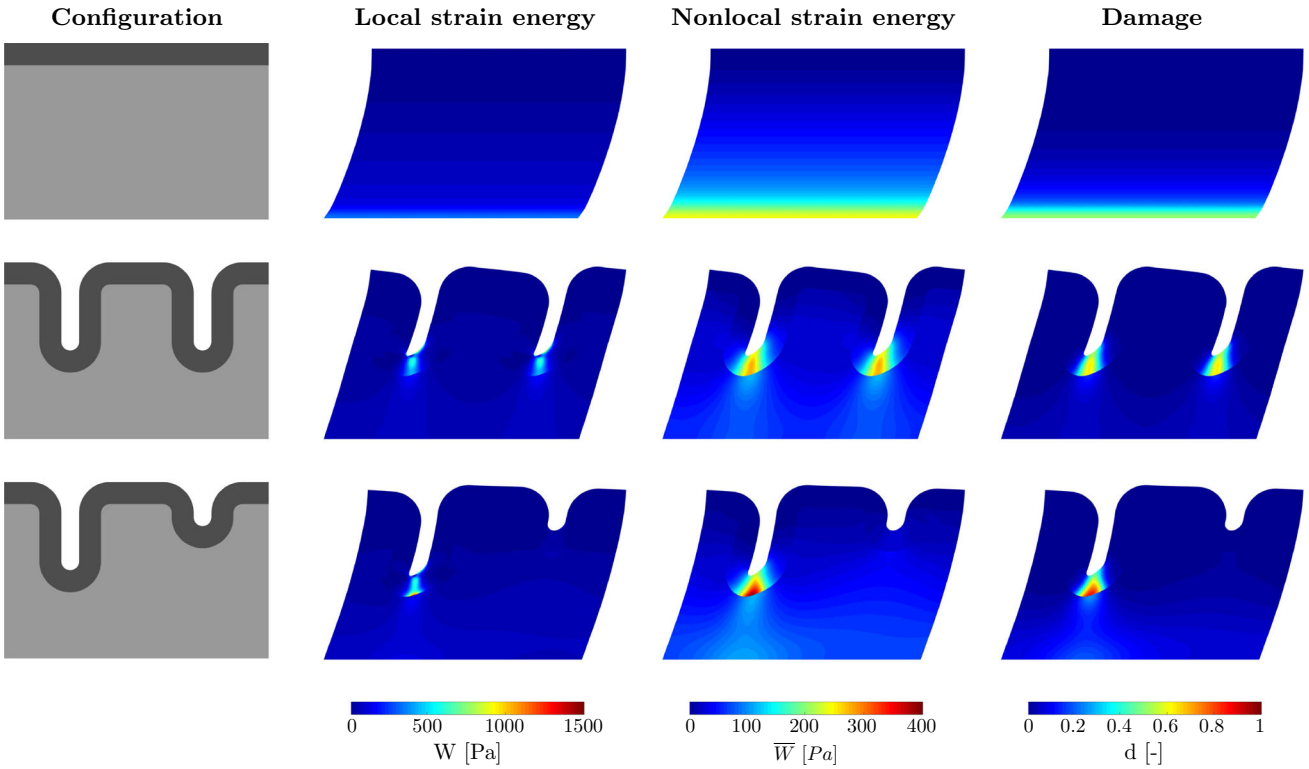

Fig. 16 Influence of brain geometry: local strain energy, nonlocal strain energy, and damage fields for a smooth surface, for two equivalent sulci and for deep and shallow sulci during unloading

ing gyri and sulci. We calibrate the damage law based on the experimental results from the literature [2]. We focus on head acceleration loadings and study with two-dimensional model systems that mimic the characteristic convoluted geometry of the brain.

As in previous studies [16], the continuum damage framework predicts that neurodegeneration first develops in highly localized regions of the brain, see Figs. 15 and 16. In fact, driven by the convoluted geometry, the mechanical response of the brain tissue, the strain energy, is maximal at the bottom of the cerebral sulci and damage is initiated in these specific areas. These results are in accordance with post-mortem histopathology studies and could explain the location of tau aggregates and subsequent neurodegeneration during the early stages of chronic traumatic encephalopathy. We would like to note that this example focuses on the initial sites of damage, which could have been assessed equally well with existing hyperelastic models [7]. In a follow up study, we are currently using the model to explore the irreversible accumulative nature of damage by investigating the effects of multiple repeated injuries.

We investigate the influence of the mechanical properties of gray and white matters, as material interfaces are associated with a discontinuity in the strain field and might have an important effect on the mechanical response. By including a material interface between the gray matter cortex and the underlying white matter substrate, we show that damage develops and is initially restricted to the cortex, as in Figs. 13, 15 and 16. These results are also in agreement with the histopatology of chronic traumatic encephalopathy brains and could explain why tau deposition is initially constrained to the cortical layer. Although the proposed damage framework allows us to further understand and model the initial stages of chronic traumatic encephalopathy, several limitations should be addressed in future works.

A more extensive set of experimental data would help to more reliably calibrate the damage parameters. In this work, the calibration of the damage law is based on tensile tests on guinea pigs optical nerves [2]. The authors detected structural impairments of the optical nerves through staining of dead cells in the tissue. First, although we expect brain tissues to behave similarly within species, it remains to be proven that the evaluated strain thresholds are valid for human brain. Moreover, the identification of the damage thresholds was based on cell death detection, which happens later as a consequence of tau deposition [43]. Therefore, we expect lower damage thresholds for the initiation of tau aggregation in chronic traumatic encephalopathy. However, since biomarkers for chronic traumatic encephalopathy remain difficult to identify and track and since only a few experimental data sets are available so far, this parameter calibration can be viewed as a reasonable first estimation.

So far, we have considered damage to be isotropic. However, experimental results provided by diffusion tensor

imaging [31] or magnetic resonance elastography [48] show that the brain tissue microstructure is highly anisotropic. The assumption of isotropy might remain valid at the initiation stage of chronic traumatic encephalopathy, as neurodegeneration appears in highly localized and confined areas. However, the anisotropy of brain tissues, especially in the white matter regions, will certainly have a drastic impact on the transport of misfolded tau proteins [22] and should therefore be included in the model.

We assumed damage to be symmetric with respect to tension and compression. Mechanical testing suggests that brain tissue is softer in tension than in compression [6] and more likely to damage under tensile loading. Along the same lines, it is still an open question whether damage is energy driven, as we assume here, or driven by volumetric or shear deformations [12]. Studying different damage criteria would certainly allow us to further identify the type and the magnitude of loading necessary to trigger neurodegeneration.

6 Conclusion

Our proposed framework to model neurodegeneration using continuum damage mechanics can pave the way to further understand the initiation phase of chronic traumatic encephalopathy. Our simulations correctly predict the regions of initial neurofibrillary tangle deposition and brain damage located at the depth of the cerebral sulci. Our nonlocal gradient approach provides unique mesh-independent solutions with similar damage profiles and load-displacement curves irrespective of the underlying mesh size. Through independent nonlocal fields for gray and white matter tissue, damage remaines initially constrained to the cortical layer, where it gradually increases, spreads, and propagates. Our model has the potential to predict the cumulative effects of repeated mild to moderate head injuries and allows us to illustrate and investigate how chronic traumatic encephalopathy gradually affects the brain. The damage model inherently introduces irreversibility, a feature that captures the accumulating pathway of chronic neurodegeneration. Ultimately, our goal is to build on these simple model problems and generate a whole brain model to simulate the full progression of neurodegeneration. Towards this goal, a natural next step would be to couple our phenomenological damage model to a more mechanistic interpretation of damage as the result of the build-up and spreading of pathogenic tau proteins across the brain. A coupled biochemo-mechanical damage model with the biochemical concentration of pathogenic proteins and the mechanical deformation as primary unknowns could provide insight into the spatio-temporal origin and propagation of chronic traumatic encephalopathy. A better understanding of these emerging disease patterns could help identify common mechanisms of neurodegeneration in repetitive mild traumatic brain injury and dementia, and, eventually, provide new insight into the correlation between chronic traumatic encephalopathy and early aging.

Acknowledgements This study was supported by a postdoctoral fellowship from the Belgian American Educational Foundation (BAEF) and a Duesberg postdoctoral fellowship from the University of Liège to Lise Noël and by the NSF Grant CMMI 1727268 Understanding Neurodegeneration across the Scales to Ellen Kuhl.

References

1. Askes H, Aifantis EC (2011) Gradient elasticity in statics and dynamics: an overview of formulations, length scale identification procedures, finite element implementations and new results. Int J Solids Struct 48(13):1962–1990. https://doi.org/10.1016/j.ijsolstr.2011.03.006
2. Bain AC, Meaney DF (2000) Tissue-level thresholds for axonal damage in an experimental model of central nervous system white matter injury. J Biomech Eng 122(6):615–622. https://doi.org/10.1115/1.1324667
3. Barber TW, Brockway JA, Higgins LS (1970) The density of tissues in and about the head. Acta Neurol Scand 46(1):85–92. https://doi.org/10.1111/j.1600-0404.1970.tb05606.x
4. Bažant ZP, Belytschko TB, Chang T-P (1984) Continuum theory for strain softening. J Eng Mech 110(12):1666–1692. https://doi.org/10.1061/(ASCE)0733-9399(1984)110:12(1666)
5. Braak H, Del Tredici K (2011) The pathological process underlying alzheimer's disease in individuals under thirty. Acta Neuropathol 121:171–181. https://doi.org/10.1007/s00401-010-0789-4
6. Budday S, Sommer G, Birkl C, Langkammer C, Haybaeck J, Kohnert J, Bauer M, Paulsen F, Steinmann P, Kuhl E, Holzapfel G (2017) Mechanical characterization of human brain tissue. Acta Biomater 48:319–340. https://doi.org/10.1016/j.actbio.2016.10.036
7. Cloots RJH, Gervaise HMT, van Dommelen JAW, Geers MGD (2008) Biomechanics of traumatic brain injury: Influences of the morphologic heterogeneities of the cerebral cortex. Ann Biomed Eng 36(7):1203. https://doi.org/10.1007/s10439-008-9510-3
8. de Rooij R, Kuhl E (2016) Constitutive modeling of brain tissue: current perspectives. Appl Mech Rev 68:010801. https://doi.org/10.1115/1.4032436
9. de Rooij R, Kuhl E (2018a) Microtubule polymerization and cross-link dynamics explain axonal stiffness and damage. Biophys J 114:201–212. https://doi.org/10.1016/j.bpj.2017.11.010
10. de Rooij R, Kuhl E (2018b) Physical biology of axonal damage. Front Cell Neurosci 12:144. https://doi.org/10.3389/fncel.2018.00144
11. de Rooij R, Miller KE, Kuhl E (2017) Modeling molecular mechanisms in the axon. Comput Mech 59:523–537. https://doi.org/10.1007/s00466-016-1359-y
12. Elsayed T, Mota A, Fraternali F, Ortiz M (2008) Biomechanics of traumatic brain injury. Comput Methods Appl Mech Eng 197:4692–4701. https://doi.org/10.1016/j.cma.2008.06.006
13. Franceschini G, Bigoni D, Regitnig P, Holzapfel GA (2006) Brain tissue deforms similarly to filled elastomers and follows consolidation theory. J Mech Phys Solids 54:2592–2620. https://doi.org/10.1016/j.jmps.2006.05.004
14. Frost B, Jacks RL, Diamond MI (2009) Propagation of tau misfolding from the outside to the inside of a cell. J Biol Chem 284:12845–12852. https://doi.org/10.1074/jbc.M808759200
15. Garcia-Gonzaelz D, Jerusalem A (2019) Energy based mechano-electrophysiological model of CNS damage at the tissue scale.

J Mech Phys Solids 125:22–37. https://doi.org/10.1016/j.jmps.2018.12.009
16. Ghajari M, Hellyer PJ, Sharp DJ (2017) Computational modelling of traumatic brain injury predicts the location of chronic traumatic encephalopathy pathology. Brain 140(2):333–343. https://doi.org/10.1093/brain/aww317
17. Gilchrist MD, O'Donoghue D (2000) Simulation of the development of frontal head impact injury. Comput Mech 26:229–235. https://doi.org/10.1007/s004660000179
18. Goriely A, Budday S, Kuhl E (2015) Neuromechanics: from neurons to brain. Adv Appl Mech 48:79–139. https://doi.org/10.1016/bs.aams.2015.10.002
19. Harris TC, de Rooij R, Kuhl E (2018) The shrinking brain: Cerebral atrophy following traumatic brain injury. Ann Biomed Eng. https://doi.org/10.1007/s10439-018-02148-2
20. Ho J, Kleiven S (2009) Can sulci protect the brain from traumatic injury? J Biomech 42(13):2074–2080. https://doi.org/10.1016/j.jbiomech.2009.06.051
21. Jordan BD (2013) The clinical spectrum of sport-related traumatic brain injury. Nat Rev Neurol 9:222–230. https://doi.org/10.1038/nrneurol.2013.33
22. Jucker M, Walker LC (2018) Propagation and spread of pathogenic protein assemblies in neurodegenerative diseases. Nat Neurosci 21:1341–1349. https://doi.org/10.1038/s41593-018-0238-6
23. Karaman E, Isildak H, Yilmaz M, Enver O, Albayram S (2011) Encephalomalacia in the frontal lobe. J Craniofac Surg 22:2374–2375. https://doi.org/10.1097/SCS.0b013e318231e511
24. Kiefer B, Waffenschmidt T, Sprave L, Menzel A (2018) A gradient-enhanced damage model coupled to plasticity-multi-surface formulation and algorithmic concepts. Int J Damage Mech 27:253–295. https://doi.org/10.1177/1056789516676306
25. Lasry D, Belytschko T (1988) Localization limiters in transient problems. Int J Solids Struct 24(6):581–597. https://doi.org/10.1016/0020-7683(88)90059-5
26. Lemaître J (1992) A course on damage mechanics. Springer, Berlin
27. Mahnken R, Kuhl E (1999) Parameter identification of gradient enhanced damage models with the finite element method. Eur J Mech/A Solids. https://doi.org/10.1016/S0997-7538(99)00127-8
28. McKee AC, Stein TD, Nowinski CJ, Stern RA, Daneshvar DH, Alvarez VE, Lee H-S, Hall G, Wojtowicz SM, Baugh CM, Riley DO, Kubilus CA, Cormier KA, Jacobs MA, Martin BR, Abraham CR, Ikezu T, Reichard RR, Wolozin BL, Budson AE, Goldstein LE, Kowall NW, Cantu RC (2013) The spectrum of disease in chronic traumatic encephalopathy. Brain 136(1):43–64. https://doi.org/10.1093/brain/aws307
29. McKee AC, Cairns NJ, Dickson DW, Folkerth RD, Keene C Dirk, Litvan I, Perl DP, Stein TD, Vonsattel J-P, Stewart W, Tripodis Y, Crary JF, Bieniek KF, Dams-O'Connor K, Alvarez VE, Gordon WA (2016) The first ninds/nibib consensus meeting to define neuropathological criteria for the diagnosis of chronic traumatic encephalopathy. Acta Neuropathol 131:75–86. https://doi.org/10.1007/s00401-015-1515-z
30. Meaney DF, Morrison B, Bass CD (2014) The mechanics of traumatic brain injury: a review of what we know and what we need to know for reducing its societal burden. J Biomech Eng 136:021008—021008-14. https://doi.org/10.1115/1.4026364
31. Mukherjee P, Berman J, Chung S, Hess C, Henry R (2008) Diffusion tensor mr imaging and fiber tractography: theoretic underpinnings. Am J Neuroradiol 29(4):632–641. https://doi.org/10.3174/ajnr.A1051
32. Nishimoto T, Murakami S (2000) Direct impact simulations of diffuse axonal injury by axial head model. JSAE Rev 21(1):117–123. https://doi.org/10.1016/S0389-4304(99)00079-X
33. Ostwald R, Kuhl E, Menzel A (2019) On the implementation of finite deformation gradient-enhanced damage models. Comput Mech. https://doi.org/10.1007/s00466-019-01684-5
34. Peerlings RHJ, de Borst R, Brekelmans WAM, de Vree JHP (1996) Gradient enhanced damage for quasi-brittle materials. Int J Numer Methods Eng 39(19):3391–3403. https://doi.org/10.1002/(SICI)1097-0207(19961015)39:19<3391::AID-NME7>3.0.CO;2-D
35. Peerlings RHJ, Geers MGD, de Borst R, Brekelmans WAM (2001) A critical comparison of nonlocal and gradient-enhanced softening continua. Int J Solids Struct 38(44):7723–7746. https://doi.org/10.1016/S0020-7683(01)00087-7
36. Riks E (1979) An incremental approach to the solution of snapping and buckling problems. Int J Solids Struct 15(7):529–551. https://doi.org/10.1016/0020-7683(79)90081-7
37. Shetty T, Raince A, Manning E, Tsiouris AJ (2016) Imaging in chronic traumatic encephalopathy and traumatic brain injury. Sports Health 8:26–36. https://doi.org/10.1177/1941738115588745
38. Simo J, Ju J (1987a) Strain- and stress-based continuum damage models–II. Computational aspects. Int J Solids Struct 23(7):841–869. https://doi.org/10.1016/0020-7683(87)90084-9
39. Simo JC, Ju JW (1987b) Strain- and stress-based continuum damage models–I. Formulation. Int J Solids Struct 23(7):821–840. https://doi.org/10.1016/0020-7683(87)90083-7
40. Smith DH, Johnson VE, Stewart W (2013) Chronic neuropathologies of single and repetitive TBI: substrates of dementia? Nat Rev Neurol 9:211–221. https://doi.org/10.1038/nrneurol.2013.29
41. Spires-Jones TL, Stoothoff WH, de Calignon A, Jones PB, Hyman BT (2009) Tau pathophysiology in neurodegeneration: a tangled issue. Trends Neurosci 32:150–159. https://doi.org/10.1016/j.tins.2008.11.007
42. Steinmann P (1999) Formulation and computation of geometrically non-linear gradient damage. Int J Numer Methods Eng 46(5):757–779
43. van den Bedem H, Kuhl E (2017) Molecular mechanisms of chronic traumatic encephalopathy. Curr Opin Biomed Eng 1:23–30. https://doi.org/10.1016/j.cobme.2017.02.003
44. Villemagne VL, Fodero-Tavoletti MT, Masters CL, Rowe CC (2015) Tau imaging: early progress and future directions. Lancet Neurol 14(1):114–124. https://doi.org/10.1016/S1474-4422(14)70252-2
45. Waffenschmidt T, Polindara C, Menzel A, Blanco S (2014) A gradient-enhanced large-deformation continuum damage model for fibre-reinforced materials. Comput Methods Appl Mech Eng 268:801–842. https://doi.org/10.1016/j.cma.2013.10.013
46. Weickenmeier J, Kuhl E, Goriely A (2018a) The multiphysics of prion-like disease: progression and atrophy. Phys Rev Lett 121:158101. https://doi.org/10.1103/PhysRevLett.121.158101
47. Weickenmeier J, Kurt M, Ozkaya E, de Rooij R, Ovaert TC, Ehman RL, Butts Pauly K, Kuhl E (2018b) Brain stiffens post mortem. J Mech Behav Biomed Mater 84:88–98. https://doi.org/10.1016/j.jmbbm.2018.04.009
48. Weickenmeier J, Kurt M, Ozkaya E, Wintermark M, Butts Pauly K, Kuhl E (2018c) Magnetic resonance elastography of the brain: a comparison between pigs and humans. J Mech Behav Biomed Mater 77:702–710. https://doi.org/10.1016/j.jmbbm.2017.08.029
49. Xiong Y, Mahmood A, Chopp M (2013) Animal models of traumatic brain injury. Nat Rev Neurosci 14:128–142. https://doi.org/10.1038/nrn3407

Publisher's Note Springer Nature remains neutral with regard to jurisdictional claims in published maps and institutional affiliations.